The Astrophysical Journal, 965:189 (15pp), 2024 April 20 https://doi.org/10.3847/1538-4357/ad293e

A JWST Project on 47 Tucanae. Overview, Photometry, and Early Spectroscopic Results of M Dwarfs and Observations of Brown Dwarfs*

A. F. Marino[1,2], A. P. Milone[1,3], M. V. Legnardi[3], A. Renzini[1], E. Dondoglio[1], Y. Cavecchi[4], G. Cordoni[5], A. Dotter[6], E. P. Lagioia[7], T. Ziliotto[3], M. Bernizzoni[3], E. Bortolan[3], M. G. Carlos[8], S. Jang[9], A. Mohandasan[3], F. Muratore[3], and M. Tailo[1,10]

[1] Istituto Nazionale di Astrofisica - Osservatorio Astronomico di Padova, Vicolo dell'Osservatorio 5, Padova IT-35122, Italy; anna.marino@inaf.it
[2] Istituto Nazionale di Astrofisica - Osservatorio Astrofisico di Arcetri, Largo Enrico Fermi, 5, Firenze IT-50125, Italy
[3] Dipartimento di Fisica e Astronomia "Galileo Galilei" - Università di Padova, Vicolo dell'Osservatorio 3, Padova IT-35122, Italy
[4] Departament de Fisica, EEBE, Universitat Politecnica de Catalunya, Av. Eduard Maristany 16, E-08019 Barcelona, Spain
[5] Research School of Astronomy and Astrophysics, Australian National University, Canberra, ACT 2611, Australia
[6] Department of Physics and Astronomy, Dartmouth College, 6127 Wilder Laboratory, Hanover, NH 03755, USA
[7] South-Western Institute for Astronomy Research, Yunnan University, Kunming 650500, People's Republic of China
[8] Theoretical Astrophysics, Department of Physics and Astronomy, Uppsala University, Box 516, SE-751 20 Uppsala, Sweden
[9] Center for Galaxy Evolution Research and Department of Astronomy, Yonsei University, Seoul 03722, Republic of Korea
[10] Dipartimento di Fisica e Astronomia Augusto Righi, Università degli Studi di Bologna, Via Gobetti 93/2, 40129 Bologna, Italy
Received 2024 January 12; revised 2024 February 9; accepted 2024 February 12; published 2024 April 19

Abstract

James Webb Space Telescope (JWST) observations have been demonstrated to be efficient in detecting multiple stellar populations in globular clusters (GCs) in the low-mass regime of M dwarfs. We present an overview, and first results, of different projects that can be explored by using the JWST observations gathered under program GO2560 for 47 Tucanae, the first program entirely devoted to the investigation of multiple populations in very-low-mass stars, which includes spectroscopic data for the faintest GC stars for which spectra are available. Our color–magnitude diagram (CMD) shows some substructures for ultracool stars, including gaps and breaks in slope. In particular, we observe both a gap and a minimum in the F322W2 luminosity function less than 1 mag apart, and discuss which it could be associated with the H-burning limit. We detect stars fainter than this minimum, very likely brown dwarfs. We corroborate the ubiquity of the multiple populations across different masses, from $\sim$0.1 $M_{\odot}$ up to red giants ($\sim$0.8 $M_{\odot}$). The oxygen range inferred for the M dwarfs, both from the CMD and from the spectra of two M dwarfs associated with different populations, is similar to that observed for giants. We have not detected any difference between the fractions of stars in distinct populations across stellar masses $\gtrsim$ 0.1 $M_{\odot}$. This work demonstrates the JWST's capability in uncovering multiple populations within M dwarfs and illustrates the possibility to analyze very-low-mass stars in GCs approaching the H-burning limit and the brown-dwarf sequence.

Unified Astronomy Thesaurus concepts: M dwarf stars (982); Population II stars (1284); CCD photometry (208)

1. Introduction

The majority of globular clusters (GCs) harbor diverse stellar populations characterized by distinct chemical compositions. This includes a first population (1P) of stars with compositions akin to field stars exhibiting comparable metallicity, alongside one or more "second" populations (2Ps) enriched in helium, nitrogen, aluminum, and sodium, while being depleted in carbon and oxygen (e.g., Kraft 1994; Bastian & Lardo 2018; Gratton et al. 2019; Milone & Marino 2022).

Since the first discoveries, the intricate complexities underlying the coexistence of distinct stellar populations in GCs have posed a challenge to our understanding of both stellar evolution and star formation in the early Universe. In the past decades, a huge observational effort has been devoted to the study of multiple populations (MPs) in GCs and several physical processes have been proposed for their formation. However, a consensus regarding their origin is still missing (see the reviews by Renzini et al. 2015; Bastian & Lardo 2018; Milone & Marino 2022, and references therein).

The current understanding of the "observed framework" provides two main competing scenarios. According to the multiple generations scenarios, MPs are attributed to distinct bursts of star formation at different epochs. 2P stars are born from material processed and ejected by 1P stars (e.g., Cottrell & Da Costa 1981; Dantona et al. 1983; Renzini et al. 2022). Various kinds of 1P polluters have been proposed, including massive binary, asymptotic giant branch (AGB), rotating, and supermassive stars (e.g., Ventura et al. 2001; Decressin et al. 2007; de Mink et al. 2009; Krause et al. 2013; Denissenkov & Hartwick 2014; D'Antona et al. 2016; Calura et al. 2019; Lacchin et al. 2024). However, regardless of proposed polluters, the amount of available material for 2P star formation is only a small fraction of the total present-day mass of 1P stars, a challenge known as the "mass budget problem." To cope with this, 1P stars are required to be substantially more massive at their formation and the progenitors of GCs should have lost a large fraction of them, thus providing a significant contribution to the mass of the Galactic halo. In this context, it has been

* The main data set presented in this article was obtained from the Mikulski Archive for Space Telescopes (MAST) at the Space Telescope Science Institute. The specific observations analyzed can be accessed via doi:10.17909/6t82-4360.

argued that GCs would have formed inside dwarf galaxies as a result of a cooling catastrophe, with a fraction of the dwarf itself having contributed material for the formation of 2Ps (Renzini et al. 2022). As opposed to a compact, massive progenitor that would not lose much mass, a dense GC embedded in an extended envelope would easily survive tidal interaction while losing most of the envelope itself, e.g., as suggested by *N*-body simulations (Lacchin et al. 2024).

Alternatively, it has been suggested that a fraction of stars from the same generation successively accreted material processed and ejected by massive stars of their own generation (Bastian et al. 2013; Gieles et al. 2018). This scenario was proposed as an attempt to cope with the mass budget issue, assuming that a much lesser amount of processed material would be required to produce the 2Ps, compared to the multiple stellar generations case. However, if only a small amount of accreted material was sufficient to produce the 2Ps, then one would expect this material to be mixed over the whole envelope as stars reach the red giant branch (RGB), thus producing a difference in composition with respect to main-sequence (MS) stars, which is not observed. Even more fundamentally, as 2P stars are enriched in helium, the putative accreted material would have a higher mean molecular weight compared to underlying layers, thus causing Rayleigh–Taylor instabilities to mix the accreted material with most of the star. Thus, accretion seems not to solve the mass budget problem, as it hardly account for the discreteness of MPs (Renzini et al. 2015). More recently, the occurrence of stellar mergers within forming binary-rich GCs has been suggested as an explanation for the MPs observed in GCs (Wang et al. 2020).

The two scenarios (multiple stellar generations and accretion) result in different expectations for the population pattern across stellar masses. Based on the multiple generations scenario, the population pattern should be identical for stars with different masses, which means that both the high-mass and low-mass stars formed during each burst of star formation should exhibit similar chemical compositions. On the other hand, in the accretion scenario the amount of accreted material depends on stellar mass, and it is proportional to the square of the stellar mass (e.g., $\propto \mathcal{M}^2$ in the case of Bondi-like accretion; Bondi & Hoyle 1944). As very-low-mass stars are less efficient in accreting polluted material, the differences in helium, carbon, nitrogen, and oxygen abundances commonly observed among red giants would systematically decrease in the M-dwarf domain.

The predictions of the two scenarios also diverge concerning the mass function (MF) of the MPs. If the 2Ps grew out of Bondi accretion, the MF of 2Ps should be significantly flatter compared to that of 1Ps (Ballesteros-Paredes et al. 2015). In contrast, if there were multiple star formation episodes, a much less pronounced difference, if any, is expected between the MF slopes of 1P and 2P stars. As the multiple stellar population pattern across different masses is a key ingredient used to constrain the formation scenarios, a comparison of stellar population properties in the very-low-mass regime of M dwarfs with those, already known, of red giants holds the promise of shedding light on the origin of this enigmatic phenomenon.

First analyses of multiple stellar populations below the MS knee have been conducted with data from the Hubble Space Telescope (HST) for the GC NGC 2808, which already showed the occurrence of different stellar populations among low-mass stars (Milone et al. 2012b). Other GCs were successively investigated including NGC 6121 (M4; Milone et al. 2014), Omega Centauri (Milone et al. 2017a), and NGC 6752 (Milone et al. 2019). These works highlight the presence of similar chemical variations among low- and higher-mass stars, supporting the multiple generations scenario. Dondoglio et al. (2022) present an analysis of a sample of GCs below the MS knee, and provided for the first time, the MFs of MPs in NGC 2808 and M4 along a wide range of stellar masses, from $\sim$0.2 to $\sim$0.8 $M_{\odot}$, finding that the fraction of MPs does not depend on stellar mass, thus further challenging the accretion scenario. First evidence of multiple stellar populations in very-low-mass stars from JWST data has been reported for 47 Tucanae (Milone et al. 2023a), M92 (Ziliotto et al. 2023), and NGC 6440 (Cadelano et al. 2023). In this paper we exploit deep JWST data to reach well below the hydrogen-burning limit in 47 Tucanae, and into the brown-dwarf regime.

This work provides an overview of a project, mainly based on observations gathered under the JWST program GO2560. The project aims at the analysis of multiple stellar populations among very-low-mass stars, in the domain of M dwarfs, in the GC NGC 104 (47 Tucanae). Since the 1970s, the presence of multiple stellar populations with different light-element abundances in this GC has been strongly established from the analysis of bright RGB stars (e.g., Dickens et al. 1979; Bell et al. 1983; Brown et al. 1990; Briley et al. 1991). Nowadays, we know that 47 Tucanae hosts two main stellar populations of 1P and 2P stars, which have been photometrically detected along the main evolutionary phases, including the MS, supergiant branch, RGB, horizontal branch (HB), and AGB (e.g., Anderson et al. 2009; Milone et al. 2012a; Tailo et al. 2020; Lagioia et al. 2021; Jang et al. 2022; Lee 2022), and correspond to stars with different light-element abundances (Marino et al. 2019). A range $\sim$0.4 dex in [C/Fe], $\sim$0.5 dex in [O/Fe], and $\sim$1.0 dex in [N/Fe] (Carretta et al. 2009; Dobrovolskas et al. 2014; Marino et al. 2016) has been observed, whereas helium spans an interval of $\delta Y = 0.05$ in mass fraction (Milone et al. 2018b). Astrometric plus spectroscopic analysis, mostly based on RGB stars or bright MS stars, shows that these stellar populations exhibit different radial distributions and internal kinematics (e.g., Richer et al. 2013; Milone et al. 2018a; Cordoni et al. 2020).

In this work, we exploit the JWST's capabilities to explore the regime of low-mass stars in 47 Tucanae, starting from $\sim$0.1 $M_{\odot}$ and reaching the H-burning limit and beyond. First photometric data for this program, observed on 2022 July 13, have recently demonstrated the JWST's capability in uncovering MPs within the low-mass realm of M dwarfs, marking indeed a pivotal advancement in the possibility of understanding the formation and evolution of GCs (Milone et al. 2023a).

Here, we present the latest observations collected in 2023 September, including both photometric and spectroscopic data, which allowed us to explore the faintest stars of 47 Tucanae, encompassing a number of astrophysics issues, from the analysis of multiple stellar populations to the observation of brown dwarfs, and to the spectral detection of chemical variations. For the first time, we provide direct spectroscopic evidence of MPs among M dwarfs, obtained from the first spectra ever observed in the faint MS of a GC.

The overview of this work is as follows: Section 2 describes the data set while Section 3 presents the color–magnitude diagrams (CMDs) obtained from NIRCam images, and focuses

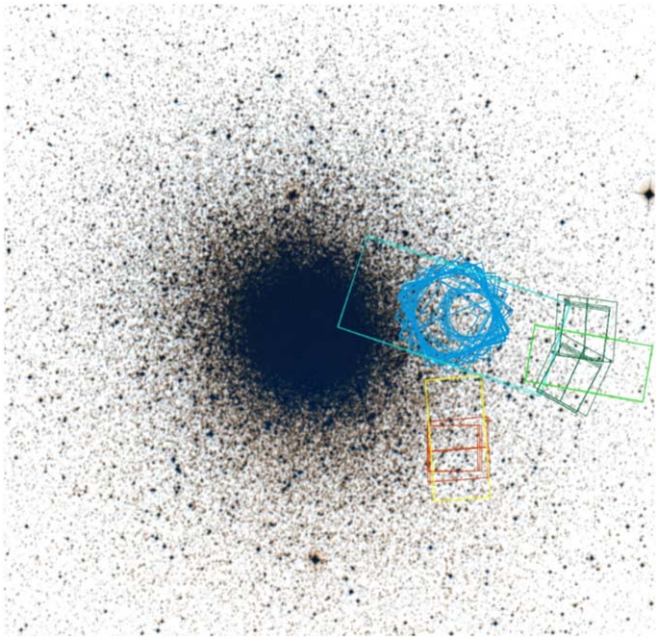

Figure 1. Footprints of the images used in our work on 47 Tucanae. Cyan and azure colors represent the JWST and HST images, respectively, of field A, whereas the JWST and HST footprints of field B are colored yellow and orange, respectively. Light and dark green colors respectively indicate JWST and HST images of field C. North is up, and east is to the left.

on very-low-mass stars, including M dwarfs and the brown dwarfs, which are poorly explored in GCs. This section includes an analysis of MPs among M dwarfs, based on the CMDs. We present in Section 4 early results based on the spectra of two M dwarfs associated with stellar populations with very different chemical compositions, and Section 5 compares the fraction of 1P and 2P stars among stars with different masses. Finally, Section 6 discusses and summarizes our results.

2. Data and Data Reduction

To investigate low-mass stars in 47 Tucanae with photometry, we used images collected with the Near-InfraRed camera (NIRCam) on board JWST, the Wide Field Channel of the Advanced Camera for Surveys (WFC/ACS), and the ultraviolet and visual channel and the infrared channel of the Wide Field Camera 3 of HST (UVIS/WFC3 and IR/WFC3). The data set consists of NIRCam images of a field, denoted as C and positioned approximately 11′ (corresponding to ∼3.5 half-light radii, assuming a half-light radius of 3.′17; Harris 1996) westward from the cluster center, (R.A. $\sim 00^{h}21^{m}16^{s}$, decl. $\sim -72^{d}06^{m}16^{s}$), which is observed as part as GO2560 (PI: A. F. Marino). We acquired images of field C simultaneously using the F115W filter of the short-wavelength channel and the F322W2 filter of the long-wavelength channel. These images were captured using the DEEP8 readout pattern and were dithered to cover the gaps between the *A* and *B* detectors of the short-wavelength channel effectively. In addition, we used data of a different field, denoted as A (R.A. $\sim 00^{h}22^{m}37^{s}$, decl. $\sim -72^{d}04^{m}06^{s}$) and located about 5′ (∼1.5 half-light radii) westward from the center of 47 Tucanae. In particular, we analyzed three regions of field A that have been observed as part of three distinct visits of JWST (GO2559, PI: I. Caiazzo).

The footprints of these images are shown in Figure 1, where we also show the images of field B (R.A. $\sim 00^{h}22^{m}36^{s}$, decl. $\sim -72^{d}09^{m}27^{s}$) studied by Milone et al. (2023a). The main properties of the JWST images of fields A and C and the HST images of field C are summarized in Table 1, whereas we refer to Milone et al. (2023a) for details on the other images of fields A and B.[11] For completeness, we note that the line-of-sight-based rotation axis of 47 Tucanae has inclination ∼ 136° north to east (Bianchini et al. 2013; Cordoni et al. 2020).

To measure stellar fluxes and positions we used a method that is based on two main steps. First-step photometry and astrometry is obtained by using the computer program *img2xym*. Originally devised by Jay Anderson (e.g., Anderson & King 2006) for the reduction of HST images, the methodology involves independently measuring stellar fluxes and positions in each image. This is achieved by employing a spatially variable point-spread function (PSF) model (Anderson & King 2000) along with a "perturbation PSF" that fine-tunes the fitting process to accommodate slight variations in the telescope focus. The perturbation PSF is obtained through unsaturated, bright, and isolated stars. All magnitude determinations derived from individual filters and cameras have been standardized to a common photometric zero-point, aligning with the zero-point of the deepest exposure in the chosen filter, which serves as the reference frame for constructing the photometric master frame. This alignment was achieved by utilizing bright, unsaturated stars well fitted by the PSF to calculate the magnitude differences between the master frame and each exposure. The mean of these differences was then used to transform star measurements in each exposure into the reference frame. For geometric distortion correction, solutions provided by Bellini et al. (2011), Anderson (2022), and Milone et al. (2023a) were applied to adjust the stellar positions in the UVIS/IR, UVIS/WFC3, and NIRCam images. The coordinates of stars in all cluster images were transformed into a common reference system based on Gaia Data Release 3 catalogs (Gaia Collaboration et al. 2021). This transformation ensures alignment with the west and north directions for the abscissa and ordinate, respectively.

The second-step photometry and astrometry of all sources has been carried out with the computer program KS2, which is developed by Jay Anderson and is based on the program *kitchen_sync* by Anderson et al. (2008; see Sabbi et al. 2016; Bellini et al. 2017; Milone et al. 2023b, for details).

KS2 employs three distinct methods for measuring stars, and each method provides optimal photometry for stars with varying levels of brightness. In method I, which works well for bright stars, the stellar fluxes and positions were independently derived in each individual exposure by using the most suitable effective PSF model for their specific location on the detector. The sky brightness is measured over an annular region between 4 and 8 pixels from the center of the star.

Method II combines information from all exposures to derive the magnitudes of stars in each exposure by means of aperture photometry, after subtracting nearby stars. Specifically, we used a 5×5 pixel aperture and determined the sky as in method I. This method works well for faint stars, which often

[11] In addition to the NIRCam data listed in Table 1, field A comprises ACS/WFC images in F606W and F814W, and IR WFC3 images in F105W, F110W, F140W, and F160W. Field B data consist of NIRCam F115W and F322W2 images collected as part of GO2560, and field B has been observed with HST in the F110W and F160W filters of the IR WFC3 camera and in F606W of UVIS/WFC3 (see Milone et al. 2023a, for further details).

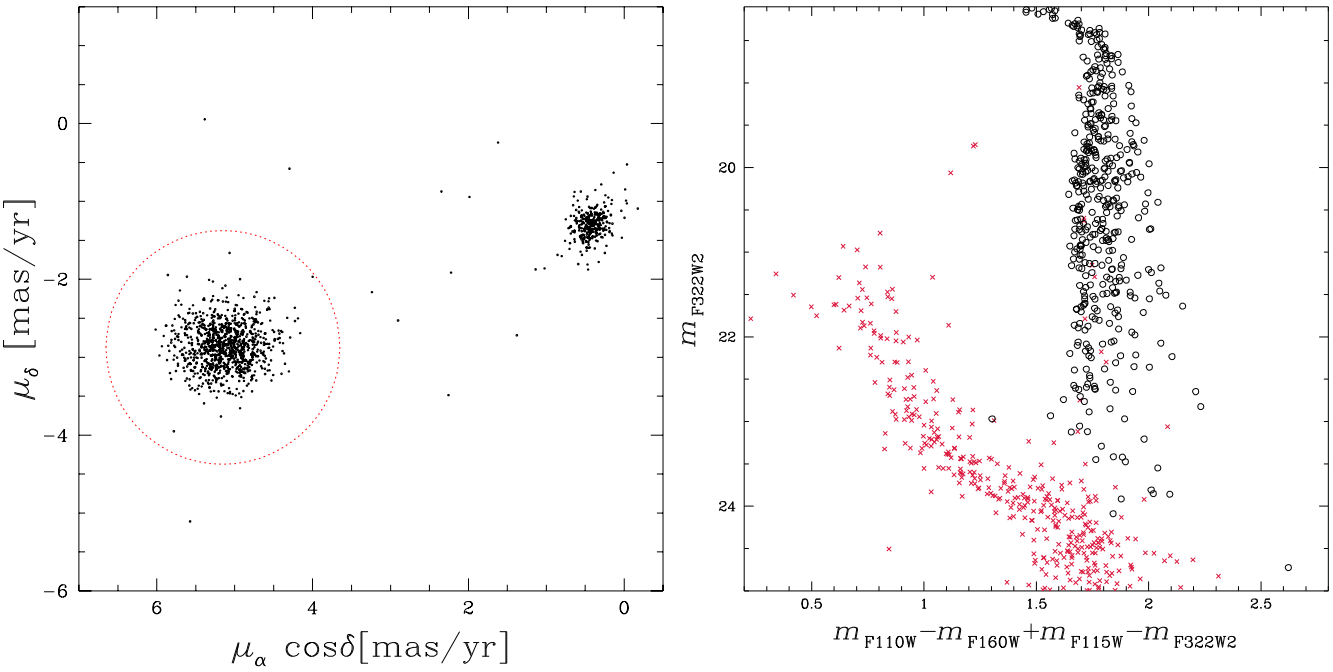

Figure 2. Left: proper motions for stars in field C brighter than $m_{F322W2} = 24.0$ mag. Stars in 47 Tucanae, within the red dotted circle, and SMC are clearly separated in this plot. Right: m_{F322W2} vs. $m_{F110W} - m_{F160W} + m_{F115W} - m_{F322W2}$ pseudo-CMD for probable cluster members (black circles), which are located within the red dotted circle in the left panel and for SMC stars (red crosses).

Table 1
Description of the Images Used in This Paper

MISSION	CAMERA	FILTER	DATE	N × EXPTIME	GO	PI
			Field A			
JWST	NIRCam	F150W2	2022 September 14	16 × 857 s	2559, Visit 1	I. Caiazzo
JWST	NIRCam	F322W2	2022 September 14	16 × 857 s	2559, Visit 1	I. Caiazzo
JWST	NIRCam	F150W2	2022 September 15	16 × 857 s	2559, Visit 2	I. Caiazzo
JWST	NIRCam	F322W2	2022 September 15	16 × 857 s	2559, Visit 2	I. Caiazzo
JWST	NIRCam	F150W2	2022 September 15	16 × 857 s	2559, Visit 3	I. Caiazzo
JWST	NIRCam	F322W2	2022 September 15	16 × 857 s	2559, Visit 3	I. Caiazzo
			Field C			
JWST	NIRCam	F115W	2023 September 24	38 × 1031 s	2560	A. F. Marino
JWST	NIRCam	F322W2	2023 September 24	38 × 1031 s	2560	A. F. Marino
HST	UVIS/WFC3	F606W	2010 April 10	2 × 50 s + 1347 s + 1398 s	11677	H. B. Richer
HST	IR/WFC3	F110W	2010 April 10	102 s + 174 s + 2 × 1399 s	11677	H. B. Richer
HST	IR/WFC3	F160W	2010 April 10	4 × 299 s + 4 × 1199 s	11677	H. B. Richer

Note. For each data set, we indicate the mission (JWST or HST), the camera, the filter, the date, the exposure times, the GO program, and the principal investigator. We also indicate the visit numbers of GO2559 observations. The observations collected during visit 1, 2, and 3 are centered around (R.A., decl.) = ($0^h22^m6.0^s$, $-72^d03^m51^s$), ($0^h22^m13.s9$, $-72^d05^m44^s$), and ($0^h23^m11.s2$, $-72^d04^m25^s$), respectively.

do not have enough photons to constrain their fluxes and positions in the individual exposures. Method III is similar to method II. The main difference is that the aperture photometry is computed by considering a circular region with a radius of 0.75 pixels, and the background sky is determined from the annulus located between 2 and 4 pixels away from the initially identified position. Subsequently, the multiple measurements for each star are averaged to obtain the most accurate estimations of their magnitudes and positions.

We used the parameters that are indicative of the astrometric and photometric quality provided by the KS2 computer programs to select the stars that are well fitted by the PSF model. To do this, we used the procedure by Milone et al. (2023b, see their Section 2.4). Photometry has been calibrated to the Vega system as in Milone et al. (2023b) and by using the zero-points available in the Space Telescope Science Institute webpage[12] for WFC3 and NIRCam. We verified that the photometry is not affected by significant reddening variations across the field of view (Legnardi et al. 2023). Hence, we did not correct the photometry for differential reddening.

Proper motions are derived as in Milone et al. (2023a, see their Section 2.3) by comparing the distortion-corrected positions of

[12] https://www.stsci.edu/hst/instrumentation/wfc3/data-analysis/photometric-calibration; https://jwst-docs.stsci.edu/jwst-near-infrared-camera/nircam-performance/nircam-absolute-flux-calibration-and-zero-points

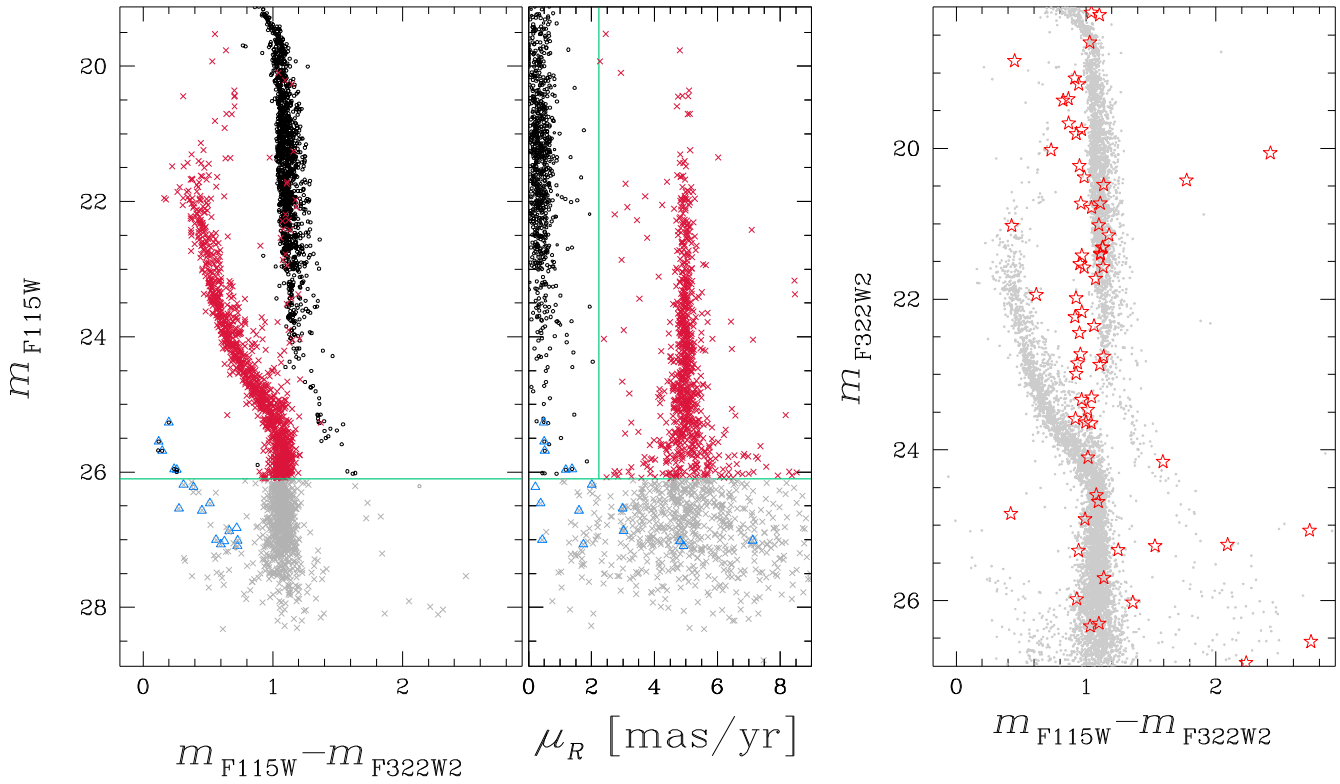

Figure 3. $m_{\rm F115W}$ vs. $m_{\rm F115W} - m_{\rm F322W2}$ CMD for stars in field C with available proper motions (left panel). The middle panel shows F115W magnitude as a function of proper motion relative to 47 Tucanae. The vertical aqua line separates the bulk of cluster members (black points in the left and middle panels) from field stars (red crosses). Stars below the aqua horizontal line, where the proper motions do not allow us to disentangle field stars from cluster members, are represented with gray crosses. Probable white dwarfs, selected from the $m_{\rm F606W}$ vs. $m_{\rm F606W} - m_{\rm F115W}$ CMD are represented with blue triangles in the left and middle panels. In the right panel we show the $m_{\rm F322W2}$ vs. $m_{\rm F115W} - m_{\rm F322W2}$ CMD for all stars in the field CMD (gray points) with the stars simulated by the trilegal Galactic model (red starred symbols; Girardi et al. 2005) for a field with the same area as field C in the direction of 47 Tucanae.

stars measured at different epochs. The proper-motion diagram derived for field-C stars brighter than $m_{\rm F322W2} = 24.0$ is plotted in the left panel of Figure 2, showcasing two primary stellar clumps encompassing the majority of cluster members and Small Magellanic Cloud (SMC) stars. The red circle is used to distinguish probable 47 Tucanae members from field stars, which are colored black and red, respectively, in the $m_{\rm F322W2}$ versus $m_{\rm F110W} - m_{\rm F160W} + m_{\rm F115W} - m_{\rm F322W2}$ pseudo-CMD.

The $m_{\rm F115W}$ versus $m_{\rm F115W} - m_{\rm F322W2}$ CMD of all stars with available proper motions is plotted in the left panel of Figure 3. We computed for each star the proper motion relative to the average proper motion of 47 Tucanae, $\mu_{\rm R}$, and plotted this quantity against the F115W magnitude. For magnitudes brighter than $m_{\rm F115W} = 26.1$ mag the stars of 47 Tucanae and the SMC exhibit distinct proper motions. Hence, we draw by eye the vertical aqua line to separate the bulk of cluster members from the field stars, which are colored black and red, respectively in the left and middle panels of Figure 2. Due to the large observational errors, the proper motions of stars fainter than $m_{\rm F115W} = 26.1$ mag do not allow us to disentangle field stars from cluster members.

To estimate the amount of faint field stars that we expect in field C, we compare the observed $m_{\rm F322W2}$ versus $m_{\rm F115W} - m_{\rm F322W2}$ CMD of all stars with available NIRCam photometry and the simulated CMD calculated by the Trilegal code (Girardi et al. 2005) for a Galactic field with the same area and the same Galactic coordinates as field C. The result is plotted in the right panel of Figure 3 where we observe that a negligible fraction of Milky Way field star interlopers are expected to contaminate the observed CMD sequences of 47 Tucanae.

2.1. Artificial Stars and Completeness

We conducted artificial star (AS) experiments to estimate the photometric uncertainties and the completeness level of our sample by using the procedure adopted in previous papers (e.g., Anderson et al. 2008). These stars were distributed across the field of view similarly to the cluster stars and along the fiducial lines of the MS of 47 Tucanae that we derived from the observed CMDs. The ASs have been reduced by using exactly the same procedure adopted for the real stars. The KS2 computer program generates the same diagnostic measurements of photometric and astrometric quality for ASs as it does for real stars. In our analysis, we considered only a subset of ASs that are relatively isolated, exhibit good PSF fitting, and show small rms values in magnitude. These ASs were selected using the same criteria we applied to real stars in our investigation.

We partitioned the NIRCam field for each field into five concentric annuli, centered on 47 Tucanae. Within each annulus, we analyzed the results of the AS experiments in N distinct 0.5 mag bins, spanning from the saturation limit to approximately one F322W2 magnitude below the faintest star that we detected. For each of the $5 \times N$ grid positions, we calculated the average completeness by comparing the number of recovered ASs with the input ASs within that particular bin.

2.2. NIRSpec Spectra

NIRSpec has been used in the multiobject spectroscopy (MOS) mode, involving a microshutter assembly configuration, which allowed us to collect 29 source spectra of sufficient

quality simultaneously, within a $3\farcm4 \times 3\farcm6$ field of view centered on field B. We choose the G235M/F170LP disperser and filter combination, which observes the wavelength range 1.66–3.07 μm, at a nominal resolving power ~ 1000.

The improved reference sampling and subtraction (IRS^2) readout mode, with the NRSIRS2 pattern, which has five frames averaged into a single group, has been employed for our MOS observations. Each source has been observed with a two-shutter nod in slitlet pattern with two identical configurations and each configuration has been executed 10 times. Each exposure was observed for 1182 s (with 16 groups per integration), for a total on-target time of 47,280 s. However, a dither of 20″ in the dispersion direction has been applied to close the detector gap. In the end, of our 29 observed stars, 17 are covered by both dither positions, and hence have all the 40 exposures, while 12 have only one dither position (20 exposures).

We have analyzed the NIRSpec 1D extracted spectra processed with the JWST Science Calibration Pipeline (Bushouse et al. 2023). While for a full analysis of the individual stars we refer to a forthcoming paper devoted to oxygen estimates, we present in this paper the results for spectra of M dwarfs with extreme chemical compositions.

3. The NIRCam Color–Magnitude Diagram of 47 Tucanae

The $m_{\rm F322W2}$ versus $m_{\rm F115W} - m_{\rm F322W2}$ CMD of stars in field C is illustrated in the lower panels of Figure 4, whereas the upper panels show portions of the NIRCam field of view. We notice that the $m_{\rm F115W} - m_{\rm F322W2}$ color broadening of the upper MS of 47 Tucanae ($m_{\rm F322W2} \lesssim 18.7$) is comparable with the broadening due to the observational errors alone. In contrast, the MS color spread for stars fainter than the MS knee is much wider than the observational errors. This phenomenon, which is due to the presence of MPs among the M dwarfs, will be further investigated in Section 3.3. In the following Section 3.1 we investigate fainter stars at magnitudes approaching the H-burning limit.

3.1. Ultracool Dwarfs

We analyze here the faintest 47 Tucanae stars appearing in the $m_{\rm F322W2}$ versus $m_{\rm F115W} - m_{\rm F322W2}$ CMD of Figure 4. In particular, we focus on the faintest portion of the CMD, composed by a plume of stars extending from the bottom of the vertical sequence (at $m_{\rm F322W2} \sim 23.3$ mag) down to $m_{\rm F322W2} \sim 27.0$ mag. This sparsely populated group of stars covers a wide color range ($\sim$2 mag) and it appears as an extension of the bluest portion of the vertical sequence composed by the cluster's M dwarfs. A quick glance at this sequence suggests that its stars, which have masses less than $\sim 0.1\ M_{\odot}$, are not continuously distributed. In particular, we notice the presence of compelling features, namely, possible clumps at $m_{\rm F322W2} \sim 23.3$, a sharp gap $\sim$24.2 mag, and a distinct change in slope at $\sim$24.5 mag (see also Figures 4 and 5).

The observed luminosity function approaches its minimum value around $m_{\rm F322W2} \sim 25.3$, and rises up toward fainter luminosities, where we observe the bright portion of the brown-dwarf sequence. As an example of the analyzed field of view, the upper-right panels of Figure 4 show a zoom in view of the stacked F322W2 and F115W images that include two probable brown dwarfs (red and blue circles).

To investigate further the lower MS of 47 Tucanae, we show in the left panel of Figure 5 a $m_{\rm F150W2}$ versus $m_{\rm F150W2} - m_{\rm F322W2}$ CMD of stars in field A. As highlighted by the Hess diagram plotted in the inset, we confirm the main gap and bend in the CMD already evident in Figure 4. In particular, this diagram clearly shows the change in the slope of the sequence of ultracool stars at $m_{\rm F322W2} = 24.5$ mag. The right panels of Figure 5 compare the $m_{\rm F322W2}$ versus $m_{\rm F150W2} - m_{\rm F322W2}$ (top) and the $m_{\rm F322W2}$ versus $m_{\rm F115W} - m_{\rm F322W2}$ CMDs (bottom) zoomed in around the bottom of the MS, which are derived from GO2559 and GO2560 data. The dashed lines, derived by eye, enclose the bulk of stars along the MS and the brown-dwarf sequence, which we marked with black circles. The colored symbols mark the stars for which photometry from both GO2559 and GO2560 is available.

The luminosity functions and MFs may provide additional information of low-mass stars in 47 Tucanae. Unfortunately, isochrones that reproduce both massive and low-mass stars in 47 Tucanae are not available to us as shown in the left panel of Figure 6, where we compare the $m_{\rm F322W2}$ versus $m_{\rm F115W} - m_{\rm F322W2}$ CMD with three isochrones. We have marked with black dots the probable cluster MS and brown dwarfs that we selected by eye, whereas the white dwarfs of 47 Tucanae and the SMC are colored gray. The red and the blue isochrones provide the best fit of 1P and 2P stars with extreme chemical composition, respectively, and comprise stars more massive than $\sim 0.1\ M_{\odot}$. These isochrones, which refer specifically to 47 Tucanae and are described in detail by Milone et al. (2023a), are extracted from the Dartmouth database (Dotter et al. 2008) and share the same age (13 Gyr), iron abundance ([Fe/H] = −0.75), and [α/Fe] = +0.4 dex. However, they have different abundances of He, C, N, and O, in such a way that the blue isochrone is enhanced in helium mass fraction by $\Delta Y = 0.04$ and in [N/Fe] by 1.2 dex, and depleted in [C/Fe] and [O/Fe] by −0.35 and 0.50 dex, respectively, relative to the red isochrone that has $Y = 0.248$, [O/Fe] = 0.4, and solar carbon and nitrogen abundances.

To derive the mass–luminosity relation for stars less massive than $\sim 0.1\ M_{\odot}$ we tentatively used the tracks by Phillips et al. (2020; brown isochrone plotted in the left panel of Figure 6), which however are based on model atmospheres and evolution models for brown dwarfs and giant exoplanets with solar metallicity. Clearly, this isochrone, which is computed for an age of 10 Gyr, does not match the brown-dwarf sequence of 47 Tucanae, and differs from those derived by Gerasimov et al. (2024) that qualitatively reproduce the observed CMDs. In a recent paper, Nardiello et al. (2023) identified 10 candidate brown dwarfs by using a $m_{\rm F322W2}$ versus $m_{\rm F115W} - m_{\rm F322W2}$ CMD of field B stars in 47 Tucanae. These stars are distributed along the isochrone of Phillips et al. (2020) and span F322W2 magnitudes between $\sim$25.2 and 25.8 mag, which are superimposed on the SMC MS, and may belong to the SMC rather than to 47 Tucanae. Accurate stellar proper motions, which are mandatory to disentangle SMC stars and possible cluster members, are not available for these very faint stars. Hence, we neither exclude nor confirm the presence of brown dwarfs in 47 Tucanae following the Phillips et al. (2020) isochrone. In the following, we only focus on the sequence of ultracool stars analyzed in this paper.

The luminosity functions of 47 Tucanae stars are plotted in the top-right and middle-right panels of Figure 6 for the stars observed with detectors A and B of the long NIRCam channels and for all stars together. Specifically, we plotted the logarithm of

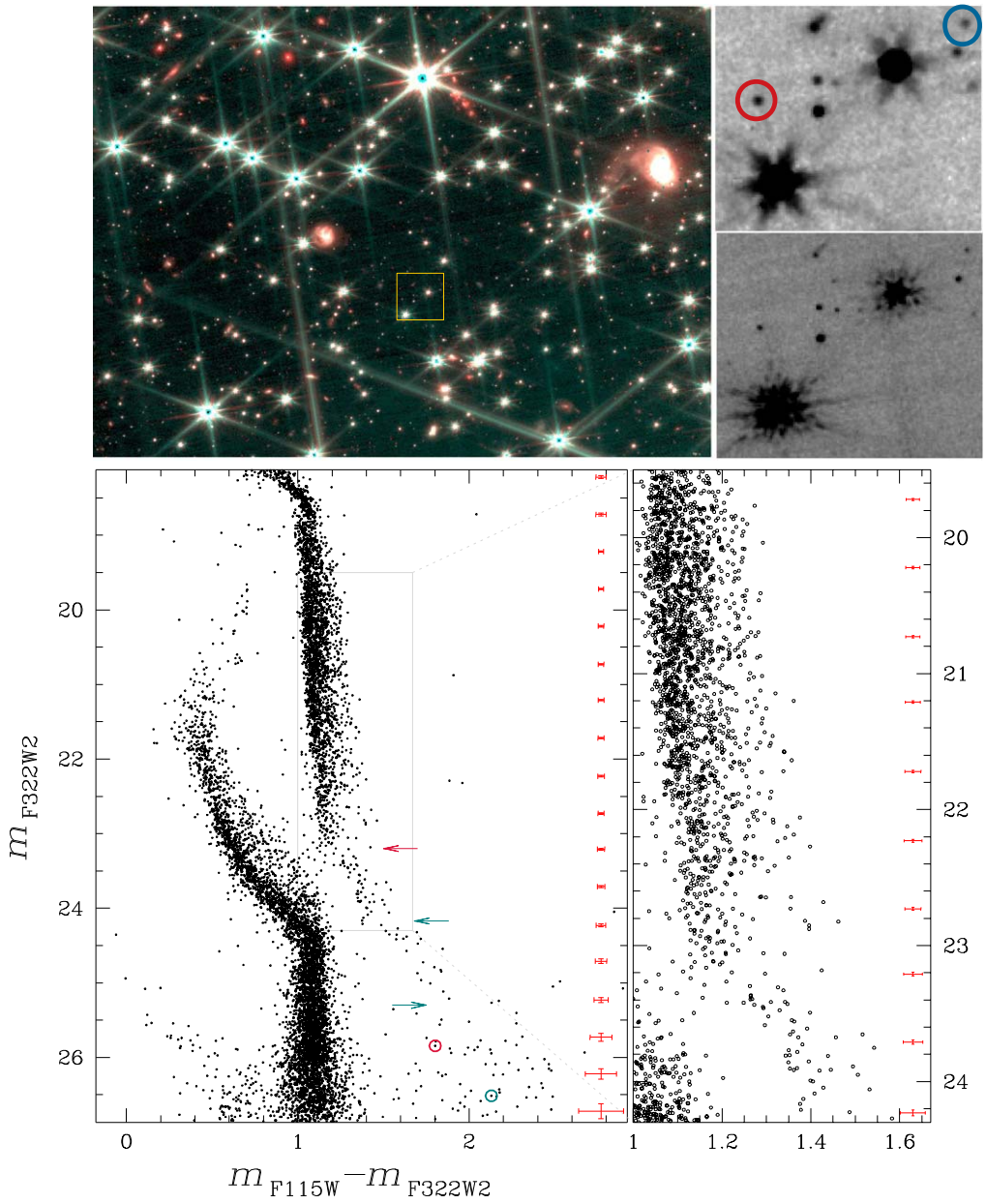

Figure 4. Top: three-color (RGB) image of a portion of the studied field of view (field C). We used the stacked F115W and F322W2 images for the B and R channels, respectively, whereas the G channel is obtained by averaging the F115W and F322W2 stacked images (left). The right panels show the F322W2 (top) and F115W (bottom) stacked images for the region within the yellow box highlighted in the field of view on the left panel. Bottom: m_{F322W2} vs. $m_{F115W} - m_{F322W2}$ CMD of stars in field C (left). The arrows indicate the location of the possible gaps or discontinuities along the sequence of ultracool 47 Tucanae stars. Stars fainter than $m_{F322W2} \sim 25.3$ mag and with colors redder than $m_{F115W} - m_{F322W2} \sim 1.5$ mag are probable brown dwarfs. The blue and red circles in the CMD highlight two of them, which are also marked in the top-right panel. We choose these two stars, among the brown-dwarf sample, for illustrative purposes, as they are located in a relatively small region of the field of view. A zoom around the MS region of 47 Tucanae populated by M dwarfs is shown in the right panel.

the numbers of stars per square arcminute, corrected for completeness, as a function of m_{F322W2} magnitude. The star counts are calculated in 0.4 mag wide bins. The luminosity function exhibits a peak around $m_{F322W2} \sim 20.2$. As we move toward fainter luminosities, the star count per unit magnitude consistently decreases, reaching a minimum around $m_{F322W2} \sim$ 25.3 mag. Beyond this point, the number of stars increases for fainter values of m_{F322W2}.

The bottom-right panel of Figure 6 shows a tentative determination of the MF, which is derived from the luminosity function plotted in the middle-right panel. For simplicity, we did not account for the MPs in 47 Tucanae, and we used the red isochrone plotted in the left panel to convert the luminosities into stellar masses for stars brighter than $m_{F322W2} \sim 22.5$, which have masses larger than $\sim$0.1 $M_{\odot}$, In this mass interval, we find that the MF exhibits a peak at $\sim$0.5 $M_{\odot}$ and declines toward lower masses.

Due to the lack of appropriate isochrones for stars with masses lower than $\sim$0.1 $M_{\odot}$, it is not possible to provide accurate MFs for these stars. Nevertheless, we assumed that the luminosity corresponding to $m_{F322W2} = 25.3$ corresponds to a stellar mass of 0.074 $M_{\odot}$, which according to Gerasimov et al. (2024) corresponds to the hydrogen-burning limit, whereas stars with $m_{F322W2} = 27$ have 0.06 $M_{\odot}$, as predicted by Gerasimov et al. (2024). The results are plotted in the bottom-right panel of Figure 6, which show an abrupt change

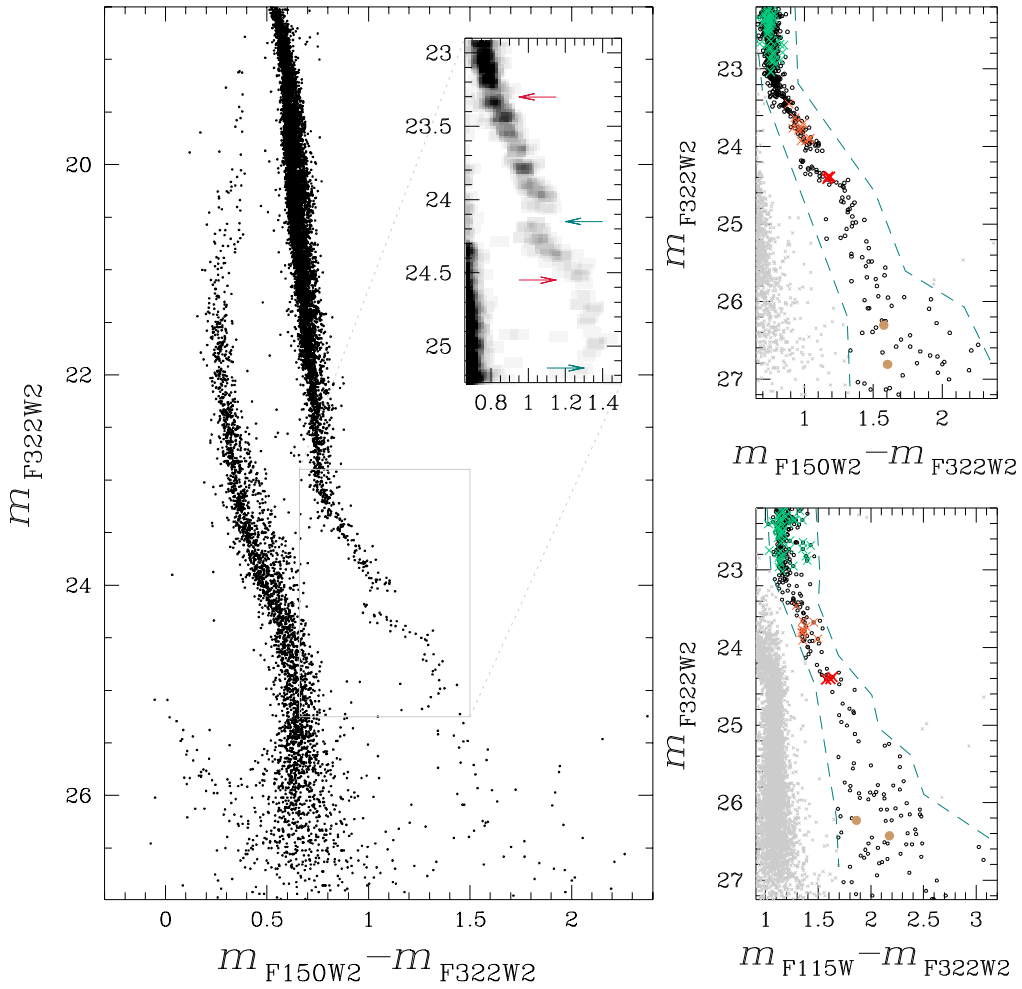

Figure 5. Left: $m_{\rm F322W2}$ vs. $m_{\rm F150W2} - m_{\rm F322W2}$ CMD of stars in field A (left). The inset shows a Hess diagram of the low MS of 47 Tucanae, where the main gaps and discontinuities are marked with colored arrows. Specifically the crimson arrows indicate the changes in slope at $m_{\rm F322W2}$ around 23.3 and 24.5 mag, while the teal arrows correspond to the sharp gap at $m_{\rm F322W2} \sim 24.2$, and the observed minimum in the luminosity function at $m_{\rm F322W2} \sim 25.3$ mag. Right: $m_{\rm F322W2}$ vs. $m_{\rm F150W2} - m_{\rm F322W2}$ (top) and $m_{\rm F322W2}$ vs. $m_{\rm F115W} - m_{\rm F322W2}$ CMDs (bottom) for faint MS stars and brown dwarfs. The stars observed in both CMDs are represented with colored symbols; specifically, the aqua, orange, and red colors indicate the dwarfs that populate the main MS segments, whereas the likely brown dwarfs observed in both data sets are colored brown.

in the MF slope at the assumed hydrogen-burning limit. We are reluctant to take for good this result, because of the tentative mass–luminosity relation we have adopted.

3.2. The M Dwarf to Brown Dwarf Transition in 47 Tucanae

As emphasized by Gerasimov et al. (2024), the termination of the hydrogen-burning MS is expected to exhibit a gap in the CMD between the faintest MS stars and the brightest brown dwarfs. Thus, it is tantalizing to identify this gap (i.e., the termination of the MS) with the evident gap at $m_{\rm F322W2} \sim 24.2$ seen in Figure 5. In their simulations Gerasimov et al. (2024) do not find a similar gap at this luminosity (their Figure 6), whereas a gap may appear at a much fainter luminosity, $m_{\rm F322W2} \sim 26$ (their Figure 10). This corresponds to the minimum in their synthetic luminosity function at this latter magnitude, as illustrated in their Figure 9. Thus, Gerasimov et al. (2024) associate this minimum with the hydrogen-burning limit.

Our observed luminosity function shows also a sharp minimum (see Figure 6), but it is found at $m_{\rm F322W2} \sim 25.3$, i.e., around half a magnitude brighter than predicted by Gerasimov et al. (2024). So, where is the hydrogen-burning limit in 47 Tucanae? Is it at $m_{\rm F322W2} \sim 24.2$, at 25.3, or at 26? What would be needed is an extended set of isochrones, possibly with options in the input physics. The data we present here represent a major jump in depth and completeness for coeval M and brown dwarfs all at the same distance and extending down to unprecedented faint luminosities. These data demand a new, parallel effort in modeling M dwarfs and brown dwarfs.

In the meantime, we can still speculate on the nature of of the gap at $m_{\rm F322W2} \sim 24.2$ and the origin of the different luminosities at the minimum of the luminosity function, just mentioned above. If the gap does not correspond to the hydrogen-burning limit, what else can cause it? These M dwarfs are fully convective, so convection effects could hardly result in such a sharp discontinuity (note that a drop is not evident in the luminosity function at this magnitude because of the binning, except in the case of the blue points in Figure 6). Could atmospheric effects cause it? We do not know, so it remains an unsolved issue.

Similarly, we cannot unambiguously pinpoint the origin of the magnitude discrepancy in the minimum of the luminosity function. Both sets use Vega magnitudes, so it cannot be a

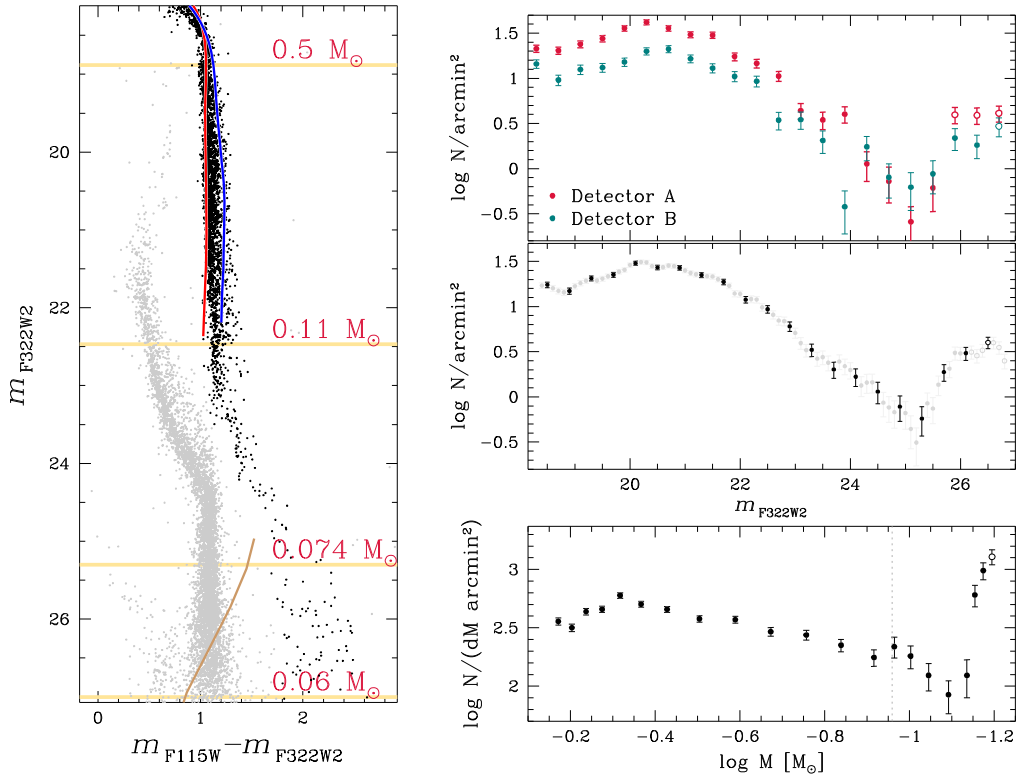

Figure 6. Left: reproduction of the $m_{\rm F322W2}$ vs. $m_{\rm F115W} - m_{\rm F322W2}$ CMD of Figure 4, where we used black colors to mark the probable MS and brown dwarfs of 47 Tucanae. We superimposed on the CMD the best-fit isochrones for MS stars (Dotter et al. 2008; Milone et al. 2023a) and the isochrone of Phillips et al. (2020) for low-mass stars. The horizontal lines mark the magnitudes corresponding to four stellar masses inferred from the red isochrone and from Gerasimov et al. (2024). Right: F322W2 luminosity function of 47 Tucanae stars along the MS and the brown-dwarf sequence obtained by using 0.4 mag wide bins. The open circles are derived from stars where the correction for the incompleteness of the photometric sample is smaller than 50%. The top panel shows the luminosity functions of stars in detectors A and B of the long-wavelength channel of NIRCam, separately, which have different radial distances $\sim 11\farcm5$ and $14\farcm5$ from the cluster center. The middle panel shows the results from the entire field of view. The gray points in the middle panel are derived by using 0.4 mag wide bins but by changing the starting magnitude value of the luminosity function by 0.1, 0.2, and 0.3 mag with respect to the value used for the black points. The bottom panel shows the MF for stars in the entire field of view. The vertical dotted line corresponds to 0.11 $M_\odot$. See the text for details.

zero-point issue. Maybe it is due to a systematic effect on the stellar models, in a regime in which a small difference in mass can result in a large difference in luminosity. On the observational side, at these faint magnitudes the luminosity function of galaxies is raising steeply, so we cannot exclude that our luminosity function of 47 Tucanae is partly contaminated by faint galaxies. Still we have excluded morphologically nonstellar objects in constructing the luminosity function of 47 Tucanae.

3.3. Multiple Stellar Populations

The $m_{\rm F322W2}$ versus $m_{\rm F115W} - m_{\rm F322W2}$ CMD in Figure 4 clearly shows that the MS color broadening, which is comparable with that expected from observational errors for stars brighter than the MS knee, suddenly increases among M dwarfs fainter than the MS knee, and approaches a value of more than 0.2 mag in the F322W2 interval between ∼20 and 23 mag.

Figure 7 provides additional information on the color distribution of MS stars. We derived by eye the aqua dashed–dotted line shown in panel (a) to define the blue boundary of the MS. Subsequently, we utilized this line to generate the verticalized $m_{\rm F322W2}$ versus $\delta(m_{\rm F115W} - m_{\rm F322W2})$ diagram represented in panel (b). To achieve this, we subtracted the color of each star from the color of the aqua fiducial associated with the identical F322W2 magnitude. Panel (c) shows the histograms and the kernel-density distributions of $\delta(m_{\rm F115W} - m_{\rm F322W2})$ in six intervals of F322W2 magnitude. The latter is obtained by using a Gaussian kernel with dispersion $\sigma = 0.02$ mag.

When considering a MS portion with nearly constant F322W2 magnitude, the majority of M dwarfs in this luminosity interval exhibit blue colors. In particular, the histograms of Figure 7(c) exhibit a peak around $\delta(m_{\rm F115W} - m_{\rm F322W2}) = 0.02$ mag, which corresponds to the bulk of 1P stars. However, there is a tail of stars that extends toward red colors.

The color broadening is mostly due to the star-to-star oxygen variations, which are associated with multiple stellar populations. The main culprit is the absorption of different chemical species containing oxygen, mainly H_2O (the primary absorber) and OH. The absorption features of these molecules strongly affect the flux in the F322W2 band whereas the F115W filter is insensitive to oxygen variations. As a consequence, the 1P stars, which have higher oxygen abundances than the 2Ps, exhibit fainter F322W2 magnitudes and bluer $m_{\rm F115W} - m_{\rm F322W2}$ colors than stars with similar atmospheric parameters (Milone et al. 2012b, 2023a; Dotter et al. 2015; VandenBerg et al. 2022; Ziliotto et al. 2023).

To quantify the amount of oxygen that is needed to reproduce the $m_{\rm F115W} - m_{\rm F322W2}$ MS broadening, we compared isochrones with different oxygen abundances (Dotter et al. 2008; Milone et al. 2023a) with the observed CMD. Specifically, we considered the isochrones with [O/Fe] = 0.4 and [O/Fe] = −0.1. To compare the

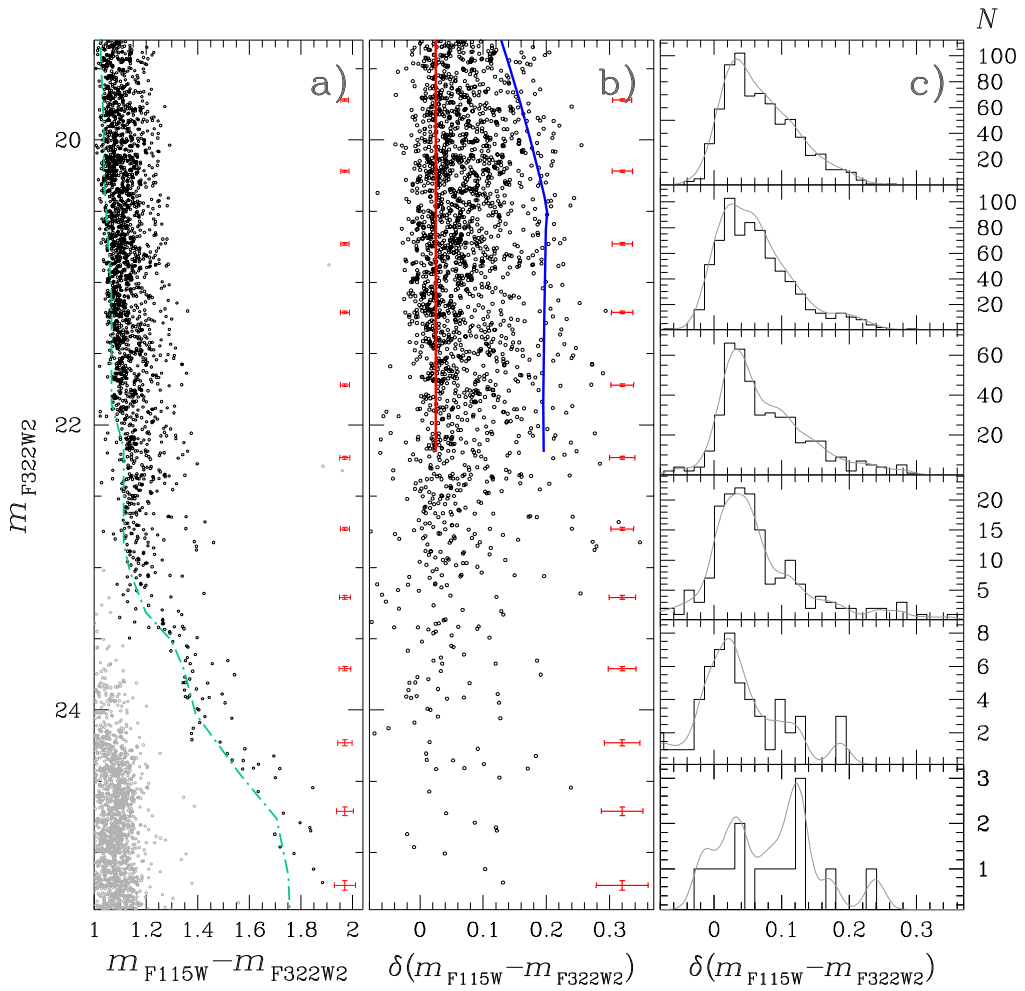

Figure 7. Reproduction of the m_{F322W2} vs. $m_{F115W} - m_{F322W2}$ CMD of Figure 4 zoomed in around the bottom of the MS of 47 Tucanae (panel (a)). The aqua line is the blue boundary of the MS and is used to derive the m_{F322W2} vs. $\delta(m_{F115W} - m_{F322W2})$ verticalized diagram shown in panel (b). The red and blue lines are the best-fit isochrones for MS stars with [O/Fe] = 0.4 and [O/Fe] = −0.1 dex, respectively (Dotter et al. 2008; Milone et al. 2023a). Panel (c) illustrates the $\delta(m_{F115W} - m_{F322W2})$ histogram distributions for stars in six F322W2 magnitude intervals and the corresponding kernel-density distributions.

relative colors of the 47 Tucanae stars with those of the isochrones properly, we have calculated the color difference between the O-poor isochrone and the O-rich one and shifted both verticalized isochrones by $\delta(m_{F115W} - m_{F322W2}) = 0.02$ mag, in such a way that the red isochrone is superimposed on the bulk of 1P stars. The $\delta(m_{F115W} - m_{F322W2})$ interval spanned by stars brighter than $m_{F322W2} \sim 22.5$ mag, which have masses larger than $\sim 0.1\ M_{\odot}$, is consistent with an oxygen variation ∼0.5 dex, comparable with the [O/Fe] range inferred for RGB stars from high-resolution spectroscopy (e.g., Carretta et al. 2009; Dobrovolskas et al. 2014). We conclude that the stars in the mass interval between ∼0.1 and 0.9 $M_{\odot}$ span a similar range of [O/Fe].

Intriguingly, as noticed by Milone et al. (2023a) for the stars in field B, the MS color broadening of stars fainter than $m_{F322W2} \sim 23$ mag appears to be much smaller than that observed for brighter M dwarfs in the F322W2 magnitude range ∼20.0–22.5. Unfortunately, there are no available isochrones that account for multiple stellar populations among ultracool stars. Hence, we cannot provide a firm conclusion on whether or not this fact is due to the lack of stellar populations with extreme chemical composition among these very-low-mass stars. Additional qualitative information on MPs among stars less massive than $\sim 0.1\ M_{\odot}$ is provided by the visual comparison between the observed m_{F322W2} versus $m_{F150W2} - m_{F322W2}$ CMD shown in Figure 5 and the CMD simulated by Gerasimov et al. (2024, see their Figure 10), which accounts for the chemical compositions of the MPs of 47 Tucanae. The simulated CMD exhibits a wide $m_{F150W2} - m_{F322W2}$ color range ∼0.5 mag for stars with $m_{F322W2} \sim 24$ mag, which seems in contrast with the narrow sequence of ultracool stars with similar luminosity observed in Figure 5. This fact suggests a possible lack of very O-poor 2P stars among ultracool stars.

Additional information on MPs in 47 Tucanae is provided by the m_{F814W} versus $C_{F606W,F814W,F322W2}$ pseudo-CMD of the stars in field B shown in the top panel of Figure 8. In this diagram, the stars fainter than the MS knee, identified at approximately $m_{F814W} = 20.0$ mag, reveal hints of four discrete sequences. According to the isochrones provided by Dotter et al. (2008) and Milone et al. (2023a), which consider the chemical composition of MPs, the reddest sequence is composed of 1P stars, while the 2P stars with particularly extreme chemical compositions display bluer $C_{F606W,F814W,F322W2}$ pseudocolors.

To maximize the information on MPs, we combine the m_{F814W} versus $C_{F606W,F814W,F322W2}$ pseudo-CMD and the m_{F814W} versus $m_{F606W} - m_{F814W}$ CMD of M dwarfs with $21.5 < m_{F814W} < 24.0$ mag. The inset of Figure 8 shows the resulting $\Delta_{CF606W,F814W,F322W2}$ versus $\Delta_{F606W,F814W}$ chromosome map (ChM), where 1P stars are clustered in the ChM

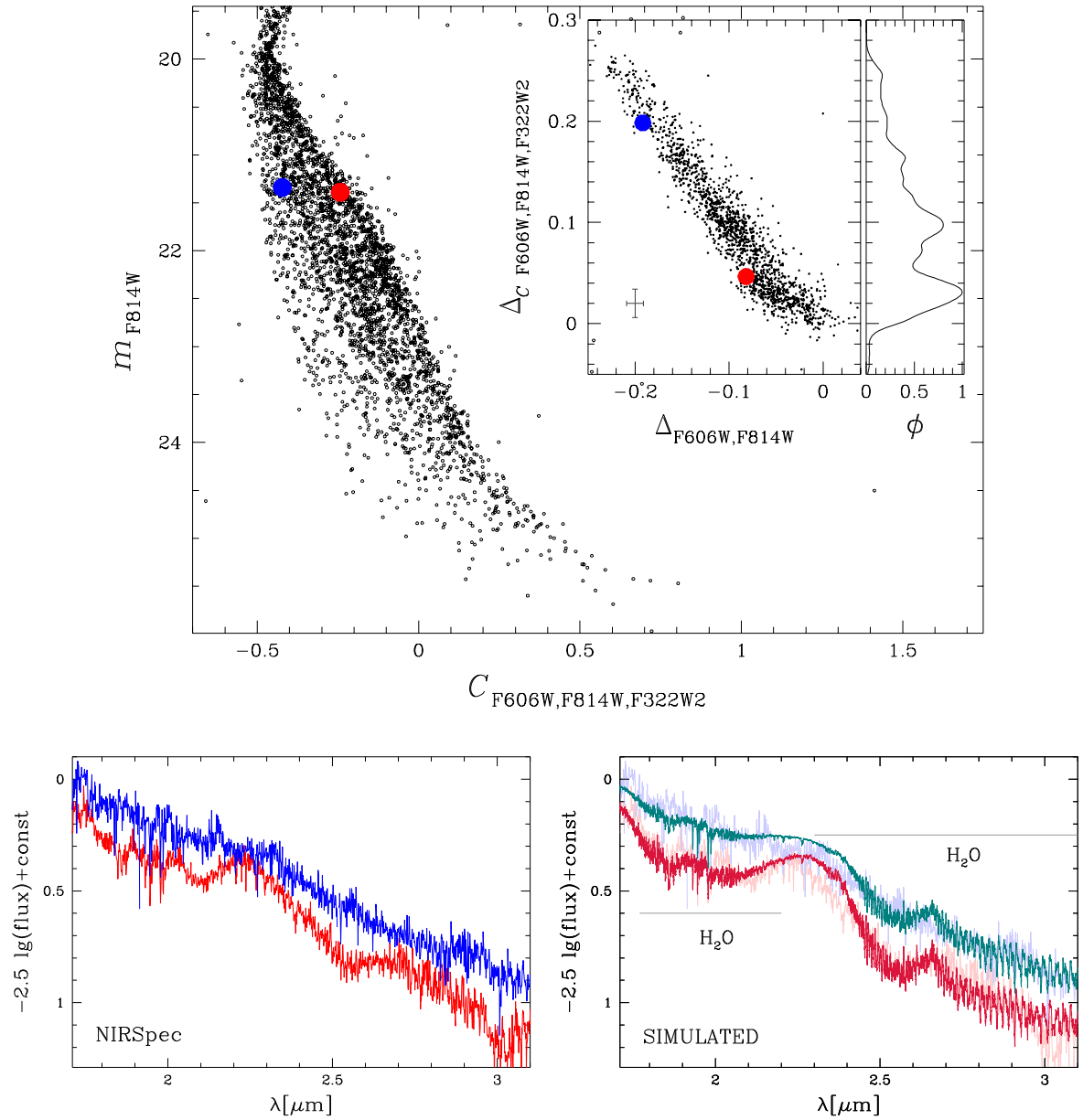

Figure 8. Top: $m_{\rm F814W}$ vs. $C_{\rm F606W,F814W,F322W2}$ pseudo-CMD for stars in field B. The inset shows the $\Delta_{C\rm F606W,F814W,F322W2}$ vs. $\Delta_{\rm F606W,F814W}$ ChM for MS stars with $21.5 < m_{\rm F814W} < 24.0$ mag, and the corresponding $\Delta_{C\rm F606W,F814W,F322W2}$ kernel-density distribution. Bottom: NIRSpec spectra for the two stars marked with large dots in the pseudo-CMD and in the ChM (left). Two simulated spectra with [O/Fe] = +0.3 (red) and [O/Fe] = −0.1 (blue) are superimposed on the observed spectra in the bottom-right panel.

region with $C_{\rm F606W,F814W,F322W2} \lesssim 0.05$ mag. We detect an extended 1P sequence that we associate with star-to-star metallicity variations, as found by Marino et al. (2023) based on high-resolution spectroscopy of RGB stars (see also Milone et al. 2017b; Legnardi et al. 2022; Milone et al. 2023a). The 2P sequence exhibits hints of four groups of stars clustered around $\Delta_{\rm F606W,F814W} \sim -0.10$, -0.14, -0.17, and -0.20 mag.

4. The Chemical Composition of M Dwarfs from NIRSpec Spectra

In this section we present NIRSpec spectra for two M dwarfs photometrically associated with different stellar populations. The location of these stars in the photometric diagrams is shown in Figure 8. The large dots superimposed on the pseudo-CMD and the ChM of Figure 8 mark indeed two stars with comparable F814W magnitudes. However, these stars exhibit distinct values for $\Delta_{C\rm F606W,F814W,F322W2}$ and $\Delta_{\rm F606W,F814W}$. Based on their location in Figure 8, upper panel, the 1P and 2P stars are labeled as red dots and blue dots, respectively.

The two targets have been spectroscopically observed as part of GO2560, and their NIRSpec spectra are displayed in the bottom-left panel of Figure 8. The red spectrum represents the star with R.A. $= 0^{\rm h}22^{\rm m}22.14^{\rm s}$ and decl. $= -72^{\rm d}04^{\rm m}10.s5$ while the blue spectrum correspond to the star with R.A. $= 0^{\rm h}22^{\rm m}12.36^{\rm s}$ and decl. $= -72^{\rm d}04^{\rm m}30.s8$. In presenting the spectra, we applied the same shift to both, plotting them such that the average value of -2.5 $\log_{10}$(flux) in the region with $\lambda < 1.75$ μm for the blue spectrum equals zero.

Clearly, the spectrum of the 1P star exhibits much stronger molecular bands than that of the 2P star. In principle, such large differences in the spectra could be either due to different

atmospheric parameters or to different chemical compositions. The location of the two stars at similar m_{F814W} magnitudes suggests that they have similar atmospheric parameters. Indeed, by fitting the m_{F814W} versus $m_{F606W} - m_{F814W}$ CMD with the isochrones of Dotter et al. (2008) and Milone et al. (2023a) we obtain $T_{eff}/\log g = 3700/5.0$ and $3600/5.0$ for the blue and the red star, respectively. Such a small difference in the atmospheric parameters alone cannot account for the differences of the observed spectra.

As outlined in the spectra of Figure 8, the main molecular features appearing in the observed spectral range are due to rotational–vibrational H_2O band heads at 1.9 and 2.7 μm, and some contribution from the CO second-overtone bands are rather masked by the H_2O bands. The water vapor molecular bands in the near-infrared are good indicators of oxygen abundance.

While for a full detailed spectroscopic analysis of all the observed NIRSpec spectra we refer the reader to an upcoming paper, here we illustrate two synthetic spectra constructed with the atmospheric parameters assumed for our two M dwarfs to infer a first estimate of the O range in the low-mass regime of 47 Tucanae. The bottom-right panel of Figure 8 shows a comparison of the observed spectra with simulated spectra with different light-element abundances. The simulated spectra are derived as in our previous works (Milone et al. 2023a; Ziliotto et al. 2023). In a nutshell, we calculated the model atmospheres using the ATLAS 12 computer program, employing the opacity-sampling technique and assuming local thermodynamic equilibrium (Kurucz 1970; Sbordone et al. 2004). We incorporated molecular line lists for all diatomic molecules listed on Kurucz's website, in addition to including H_2O molecules from Partridge & Schwenke (1997). We used the SYNTHE computer program (Kurucz & Avrett 1981; Castelli 2005; Kurucz 2005; Sbordone et al. 2007) to compute the spectra in the region between 1.7 and 3.2 μm covered by the available NIRSpec spectra. Specifically, the crimson spectrum has oxygen content $[O/Fe] = 0.3$ dex, whereas the teal one has $[O/Fe] = -0.1$ dex. Noticeably, the blue spectrum has higher effective temperature than the red one by 70 K. This effective temperature difference is consistent with the fact that the 2P stars of 47 Tucanae are helium enhanced with respect to the 1Ps (e.g., Milone et al. 2018b; Lagioia et al. 2018).

We conclude that the comparison of the spectra of the two M dwarfs belonging to different stellar populations indicates that M dwarfs exhibit a range in O abundances very similar to that reported in the literature for higher-mass stars along the RGB. The result presented here is the first detection of the O range directly performed on stellar spectra of M dwarfs, and strongly corroborates our previous findings about the similarity of the multiple stellar populations in stars with different masses (from the RGB to M dwarfs), already suggested by photometric diagrams.

5. Population Ratios

To derive the fraction of stars in the main stellar populations of 47 Tucanae we started using the $\Delta_{F110W,F160W,F115W,F322W2}$ versus $\Delta_{F606W,F110W}$ ChM of stars in field C, which is derived from the m_{F322W2} versus $m_{F110W} - m_{F160W} + m_{F115W} - m_{F322W2}$ pseudo-CMD plotted in Figure 2 and the m_{F322W2} versus $m_{F606W} - m_{F110W}$ CMD.

The results are plotted in the left panel of Figure 9. The 1P stars are clustered around the origin of the ChM, while the 2P defines a sequence ranging from $(\Delta_{F606W,F110W}, \Delta_{F110W,F160W,F115W,F322W2}) \sim (-0.2, 0.1)$ toward the top left corner of the ChM.

To assess the proportion of stars within each population, we expanded upon the approach outlined by Zennaro et al. (2019) to derive the fraction of stars in the four stellar populations of the GC NGC 2419 and apply it to the ChM of 47 Tucanae (see also Milone et al. 2012a; Nardiello et al. 2018; Milone et al. 2020). In a nutshell, we estimated the mean values of $\Delta_{F606W,F110W}$ and $\Delta_{F110W,F160W,F115W,F322W2}$ for the stars within each population (depicted as colored dots in Figure 9). In the case of 1P stars, we used two values for the center to account for subpopulations with different metallicity (Legnardi et al. 2022; Marino et al. 2023). These values served to define five distinct regions denoted as R_1, R_{2A}, R_{2B}, R_{2C}, and R_{2D} and delimited by the colored solid lines. Owing to photometric errors, each region may encompass stars from all populations. As an example, the observed count of stars within region R1 is:

$$N_{R1} = N_{1P} f_{1P}^{R1} + N_{2PA} f_{2PA}^{R1} + N_{2PB} f_{2PB}^{R1} + N_{2PC} f_{2PC}^{R1} + N_{2PD} f_{2PD}^{R1}, \quad (1)$$

where N_{1P}, N_{2PA}, N_{2PB}, N_{2PC}, and N_{2PD}, are, respectively, the numbers of 1P, $2P_A$, $2P_B$, $2P_C$, and $2P_D$ stars in each population in our sample.

The number of stars within the regions R_{2A}, R_{2B}, R_{2C}, and R_{2D} are linked to the fraction of stars of each population through four comparable equations. The values of N_{R1}, N_{R2A}, N_{R2B}, N_{R2C}, and N_{R2D} used in these equations are derived by counting the stars within the corresponding region.

The fractions of 1P, $2P_A$, $2P_B$, $2P_C$, and $2P_D$ stars within the region R1, f_{1P}^{R1}, f_{2PA}^{R1}, f_{2PB}^{R1}, f_{2PC}^{R1}, and f_{2PD}^{R1} are derived from simulated ChMs composed of ASs, and we did the same for inferring the fractions of stars of each populations in the regions of the ChM R_{2A}, R_{2B}, R_{2C}, and R_{2D}. To do this, we simulated 50,000 ASs for each population, disposed along the centers of each population in the ChM.

The numbers of stars in the five populations of 47 Tucanae, N_{1P}, N_{2PA}, N_{2PB}, N_{2PC}, N_{2PD}, are calculated by solving for these five equations. The results are provided in Table 2, where we also provide the fractions of stars in the five stellar populations that we obtain by extending the same procedure to the ChM shown in Figure 8 for stars in field A. In particular, we find that 1P stars comprise $38.1\% \pm 1.2\%$ and $46.3\% \pm 4.2$ % of the total number of ChM stars of field A and field C, respectively.

The fraction of 2P stars in 47 Tucanae inferred from either RGB or HB stars significantly changes as a function of radial distance. It ranges from about 80% near the cluster center to less than 60% for distances larger than $\sim 5'$ (Milone et al. 2012b, 2017b; Cordero et al. 2014; Dondoglio et al. 2021; Lee 2022). Figure 10 compares the fractions of 2P stars derived by Dondoglio et al. (2021) from HB stars with different radial distances (black points) and those obtained in this paper from M dwarfs (red triangles). We conclude that there is no significant difference between the fractions of 2P stars derived from stars with different masses. In the context of the multiple generations scenario, where the 2P stars form in the dense cluster center, this would imply that the initial mass function does not depend on the density of the environment.

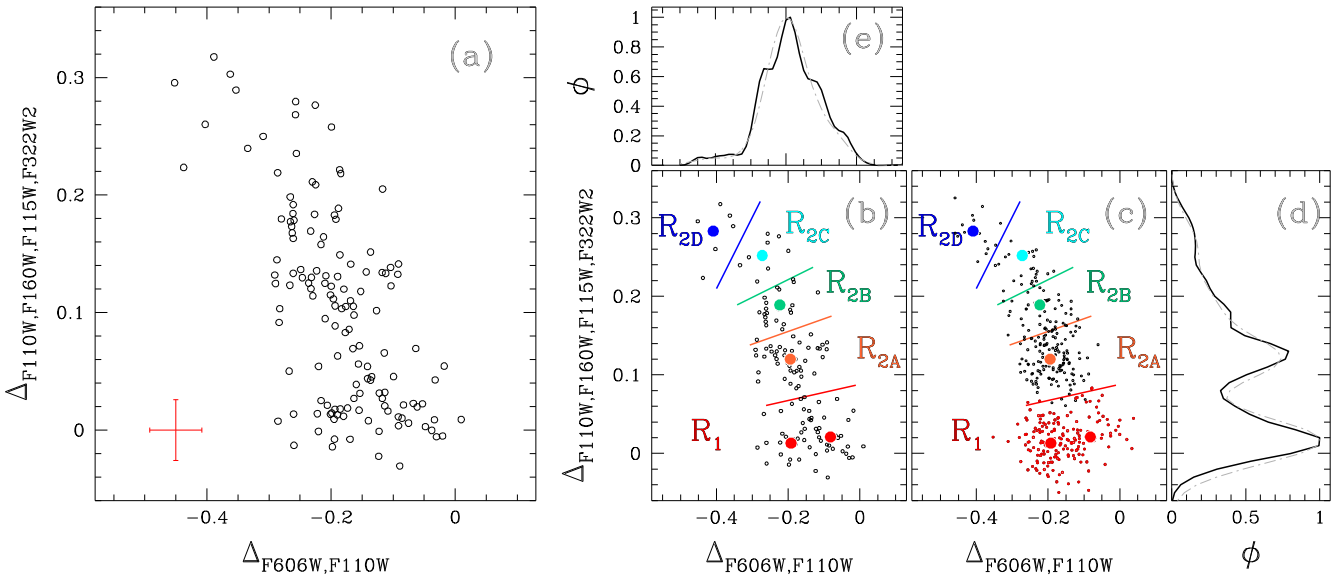

Figure 9. $\Delta_{F110W,F160W,F115W,F322W2}$ vs. $\Delta_{F606W,F110W}$ ChM of M dwarfs in field C (panel (a)). Panels (b)–(e) illustrate the procedure used to estimate the fractions of 1P and 2P stars. The observed ChM is further reproduced in panel (b), while panel (c) shows the simulated ChM where simulated 1P stars are colored in red. The colored solid lines delimit the four regions used to infer the fraction of stars in each population, while the colored dots mark the average positions in the ChM of the simulated stellar populations. Panels (d) and (e) show the $\Delta_{F110W,F160W,F115W,F322W2}$ and $\Delta_{F606W,F110W}$ kernel distributions for the observed (black line) and the simulated (gray line) stars.

Table 2
Fractions of Stars in the Five Stellar Populations of 47 Tucanae in Fields A and C

Field	1P	$2P_A$	$2P_B$	$2P_C$	$2P_D$
A	0.381 ± 0.012	0.352 ± 0.012	0.148 ± 0.009	0.065 ± 0.006	0.054 ± 0.006
C	0.463 ± 0.042	0.329 ± 0.035	0.122 ± 0.028	0.049 ± 0.021	0.036 ± 0.014

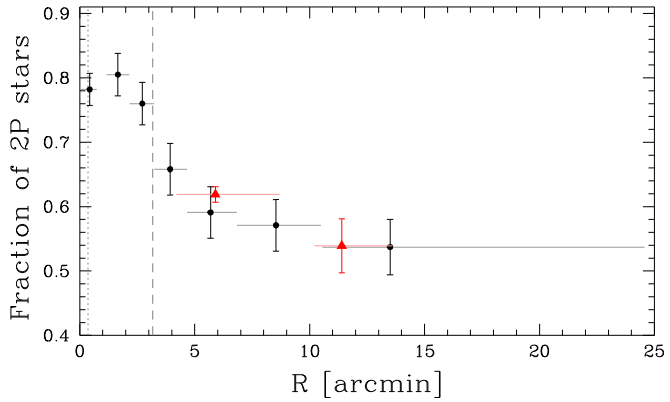

Figure 10. Fraction of 2P stars as a function of the radial distance from the cluster center. The dlack dots are derived by Dondoglio et al. (2021) by using HB stars, whereas the results obtained in this paper from M dwarfs are represented with red triangles. The horizontal lines mark the radial interval associated with each point. The dotted and dashed vertical lines mark the core and the half-light radius from the 2010 version of the Harris (1996) catalog.

6. Summary and Conclusions

We have presented our JWST project on multiple stellar populations in the GC 47 Tucanae. Our main data set comprised ∼13 hr of observing time with NIRSpec + NIRCam parallel observations, allowing us to infer crucial constraints on the MP phenomenon both from spectroscopic and photometric analysis. This is the first project specifically devoted to the analysis of multiple stellar populations in GCs conducted with the JWST. However, in addition to studies on MPs, we demonstrated that our data set has the potential to be used to investigate the general properties of poorly explored stellar populations, such as M dwarfs and brown dwarfs. In this work, we present early results which allowed us to study low-mass stars, in the domain of M dwarfs and beyond, down to the hydrogen-burning limit and the brown-dwarf sequence.

This overview sheds light on the MPs among the low-mass stars of 47 Tucanae. The main results can be summarized as follows.

1. The photometric diagrams constructed with the F322W2 filter of NIRCam, including the m_{F322W2} versus $m_{F115W} - m_{F322W2}$ CMD and the m_{F322W2} versus $C_{F606W,F814W,F322W2}$ pseudo-CMD, reveal that, below the knee, MS stars with masses larger than ∼0.1 $M_\odot$ and similar F322W2 luminosities span a wide color, or pseudocolor, range. This result corroborates the evidence of multiple stellar populations among M dwarfs (see, e.g., Dondoglio et al. 2022; Milone & Marino 2022; Milone et al. 2023a; Cadelano et al. 2023, for previous photometric studies of MPs among very-low-mass stars in 47 Tucanae).
2. The comparison between isochrones with different chemical compositions and the observed CMD reveals that the MS color broadening observed among M dwarfs more massive than ∼0.1 $M_\odot$ is consistent with stellar populations with different oxygen abundances. The [O/Fe] range ∼0.5 dex that is needed to reproduce the

observations is comparable with that observed among RGB stars by means of high-resolution spectroscopy. We notice that the $m_{F115W} - m_{F322W2}$ color broadening of very faint stars ($m_{F322W2} > 23$) appears to be narrower than that observed among the M dwarfs with brighter luminosity, similar with what was observed by Milone et al. (2023a) for stars in field B. An appropriate comparison with isochrones that account for the chemical compositions of MPs is needed to associate this fact with the possible lack of stellar populations with extreme chemical compositions among ultracool stars.

3. We present the NIRSpec spectra for two stars with similar F814W magnitudes that occupy extreme positions in the ChM and are associated with the populations 1P and $2P_C$ stars. For a fixed wavelength, the 1P star spectrum is more absorbed than the spectrum of the $2P_C$ star. The comparison with synthetic spectra with different chemical compositions reveals that the two stars have different oxygen abundances, with the $2P_C$ M dwarf being depleted by [O/Fe] = 0.4 dex with respect to the 1P star. Hence, the flux difference can be attributed to molecules consisting of oxygen (predominantly H_2O), which exhibit strong absorption in the spectra of 1P stars, known for their oxygen-rich composition. This outcome represents the first spectroscopic determination of the chemical composition of M dwarfs within a GC. It validates the earlier prediction, derived from synthetic spectra, that the observed color variation among M dwarfs in GCs is attributable to multiple stellar populations characterized by varying oxygen abundances (Milone et al. 2012b).
4. The 2P M dwarfs consist ∼62% and 54% of the total number of M dwarfs, respectively at ∼5′ and ∼11′ from the cluster center. These values are similar to the fraction of 2P stars measured among HB and RGB stars with similar radial distances (Milone et al. 2012b; Dondoglio et al. 2021), thus indicating that the fraction of 2P stars does not depend on stellar mass, at least for stars more massive than ∼0.1 $M_\odot$. This result, together with the evidence that M dwarfs and giant stars span a similar range of [O/Fe], provides a serious challenge to the scenarios for the formation of MPs that are based on accretion.

The deep NIRCam photometry collected as part of GO2560 has allowed us to detect objects in the field of 47 Tucanae down to $m_{F322W2} = 27.0$. We have thus explored the faintest MS and brown-dwarf regions, which are poorly investigated in GCs. The corresponding results can be summarized as follows.

1. Based on both the m_{F322W2} versus $m_{F115W} - m_{F322W2}$ and the m_{F322W2} versus $m_{F150W2} - m_{F322W2}$ CMDs, we detected a main discontinuity along the sequence of very-low-mass stars (masses smaller than ∼0.1 $M_\odot$) at $m_{F322W2} \sim 24.2$ mag. We also notice clear changes of the MS slope around $m_{F322W2} = 23.3$ and 24.5 mag.
2. The F322W2 luminosity function of MS stars exhibits a drop in the number of stars around $m_{F322W2} = 25.3$ mag, and the number of stars per magnitude interval rises up at fainter luminosities. We tentatively associate this gap with the hydrogen-burning limit. Hence, the deep CMD obtained from GO2560 photometry unveils, for the first time in a GC, the brown-dwarf cooling sequence.

We can conclude by emphasizing that the initial observations of GCs carried out with the JWST have showcased the telescope's capability to separate MPs among M dwarfs effectively and explore the properties of very-low-mass stars. These results mark the opening of new horizons in the exploration of the lower-mass regime. The heightened sensitivity of JWST to the infrared domain will be indeed instrumental in enabling an efficient and systematic exploration of cool, low-mass stars across a substantial sample of GCs. A current limitation is represented by the insufficient availability of theoretical isochrones and mass–luminosity relations down to the faint limits now reached with JWST.

Acknowledgments

We thank the anonymous referee for suggestions which improved the manuscript. This work has been funded by the European Union – NextGenerationEU RRF M4C2 1.1 (PRIN 2022 2022MMEB9W: "Understanding the formation of globular clusters with their multiple stellar generations", CUP C53D23001200006). T.Z. acknowledges support from the European Union's Horizon 2020 research and innovation program under the Marie Skodowska-Curie grant Agreement No. 101034319 and from the European Union NextGenerationEU. Y.C. acknowledges support from grant RYC2021-032718-I, financed by MCIN/AEI/10.13039/501100011033 and the European Union NextGenerationEU/PRTR. This work has been partially supported by the Spanish MINECO grant PID2020-117252GB-I00 and by the ABAUR/Generalitat de Catalunya grant SGR-386/2021. S.J. acknowledges support from the NRF of Korea (2022R1A2C3002992 and 2022R1A6A1A03053472).

Data Availability

The data underlying this article will be shared on reasonable request to the corresponding author.

ORCID iDs

A. F. Marino https://orcid.org/0000-0002-1276-5487
A. P. Milone https://orcid.org/0000-0001-7506-930X
M. V. Legnardi https://orcid.org/0000-0003-3153-1499
A. Renzini https://orcid.org/0000-0002-7093-7355
E. Dondoglio https://orcid.org/0000-0001-8415-8531
Y. Cavecchi https://orcid.org/0000-0002-6447-3603
G. Cordoni https://orcid.org/0000-0002-7690-7683
A. Dotter https://orcid.org/0000-0002-4442-5700
E. P. Lagioia https://orcid.org/0000-0003-1713-0082
T. Ziliotto https://orcid.org/0000-0001-8538-2068
M. G. Carlos https://orcid.org/0000-0003-1757-6666
S. Jang https://orcid.org/0000-0002-1562-7557
A. Mohandasan https://orcid.org/0000-0001-5182-0330
M. Tailo https://orcid.org/0000-0002-1128-098X

References

Anderson, J. 2022, AAS Meeting, 54, 206.01
Anderson, J., & King, I. R. 2000, PASP, 112, 1360
Anderson, J., & King, I. R. 2006, PSFs, Photometry, and Astronomy for the ACS/WFC ACS 2006-01, Instrument Science Report
Anderson, J., Piotto, G., King, I. R., Bedin, L. R., & Guhathakurta, P. 2009, ApJL, 697, L58
Anderson, J., Sarajedini, A., Bedin, L. R., et al. 2008, AJ, 135, 2055
Ballesteros-Paredes, J., Hartmann, L. W., Pérez-Goytia, N., & Kuznetsova, A. 2015, MNRAS, 452, 566

Bastian, N., Lamers, H. J. G. L. M., de Mink, S. E., et al. 2013, MNRAS, 436, 2398
Bastian, N., & Lardo, C. 2018, ARA&A, 56, 83
Bell, R. A., Hesser, J. E., & Cannon, R. D. 1983, ApJ, 269, 580
Bellini, A., Anderson, J., & Bedin, L. R. 2011, PASP, 123, 622
Bellini, A., Anderson, J., Bedin, L. R., et al. 2017, ApJ, 842, 6
Bianchini, P., Varri, A. L., Bertin, G., & Zocchi, A. 2013, ApJ, 772, 67
Bondi, H., & Hoyle, F. 1944, MNRAS, 104, 273
Briley, M. M., Hesser, J. E., & Bell, R. A. 1991, ApJ, 373, 482
Brown, J. A., Wallerstein, G., & Oke, J. B. 1990, AJ, 100, 1561
Bushouse, H., Eisenhamer, J., Dencheva, N., et al. 2023, JWST Calibration Pipeline v1.10.0, Zenodo, 10.5281/zenodo.7795697
Cadelano, M., Pallanca, C., Dalessandro, E., et al. 2023, A&A, 679, L13
Calura, F., D'Ercole, A., Vesperini, E., Vanzella, E., & Sollima, A. 2019, MNRAS, 489, 3269
Carretta, E., Bragaglia, A., Gratton, R., & Lucatello, S. 2009, A&A, 505, 139
Castelli, F. 2005, MSAIS, 8, 25
Cordero, M. J., Pilachowski, C. A., Johnson, C. I., et al. 2014, ApJ, 780, 94
Cordoni, G., Milone, A. P., Mastrobuono-Battisti, A., et al. 2020, ApJ, 889, 18
Cottrell, P. L., & Da Costa, G. S. 1981, ApJL, 245, L79
Dantona, F., Gratton, R., & Chieffi, A. 1983, MmSAI, 54, 173
D'Antona, F., Vesperini, E., D'Ercole, A., et al. 2016, MNRAS, 458, 2122
de Mink, S. E., Pols, O. R., Langer, N., & Izzard, R. G. 2009, A&A, 507, L1
Decressin, T., Meynet, G., Charbonnel, C., Prantzos, N., & Ekström, S. 2007, A&A, 464, 1029
Denissenkov, P. A., & Hartwick, F. D. A. 2014, MNRAS, 437, L21
Dickens, R. J., Bell, R. A., & Gustafsson, B. 1979, ApJ, 232, 428
Dobrovolskas, V., Kučinskas, A., Bonifacio, P., et al. 2014, A&A, 565, A121
Dondoglio, E., Milone, A. P., Lagioia, E. P., et al. 2021, ApJ, 906, 76
Dondoglio, E., Milone, A. P., Renzini, A., et al. 2022, ApJ, 927, 207
Dotter, A., Chaboyer, B., Jevremović, D., et al. 2008, ApJS, 178, 89
Dotter, A., Ferguson, J. W., Conroy, C., et al. 2015, MNRAS, 446, 1641
Gaia Collaboration, Brown, A. G. A., Vallenari, A., et al. 2021, A&A, 649, A1
Gerasimov, R., Burgasser, A. J., Caiazzo, I., et al. 2024, ApJ, 961, 139
Gieles, M., Charbonnel, C., Krause, M. G. H., et al. 2018, MNRAS, 478, 2461
Girardi, L., Groenewegen, M. A. T., Hatziminaoglou, E., & da Costa, L. 2005, A&A, 436, 895
Gratton, R., Bragaglia, A., Carretta, E., et al. 2019, A&ARv, 27, 8
Harris, W. E. 1996, AJ, 112, 1487
Jang, S., Milone, A. P., Legnardi, M. V., et al. 2022, MNRAS, 517, 5687
Kraft, R. P. 1994, PASP, 106, 553
Krause, M., Charbonnel, C., Decressin, T., Meynet, G., & Prantzos, N. 2013, A&A, 552, A121
Kurucz, R. L. 1970, SAO Special Report 309
Kurucz, R. L. 2005, MSAIS, 8, 14
Kurucz, R. L., & Avrett, E. H. 1981, Solar Spectrum Synthesis I. A sample atlas from 224 to 300 NM (Cambridge: Smithsonian Astrophysical Observatory)
Lacchin, E., Mastrobuono-Battisti, A., Calura, F., et al. 2024, A&A, 681, A45
Lagioia, E. P., Milone, A. P., Marino, A. F., et al. 2018, MNRAS, 475, 4088
Lagioia, E. P., Milone, A. P., Marino, A. F., et al. 2021, ApJ, 910, 6
Lee, J.-W. 2022, ApJS, 263, 20
Legnardi, M. V., Milone, A. P., Armillotta, L., et al. 2022, MNRAS, 513, 735
Legnardi, M. V., Milone, A. P., Cordoni, G., et al. 2023, MNRAS, 522, 367
Marino, A. F., Milone, A. P., Casagrande, L., et al. 2016, MNRAS, 459, 610
Marino, A. F., Milone, A. P., Dondoglio, E., et al. 2023, ApJ, 958, 31
Marino, A. F., Milone, A. P., Renzini, A., et al. 2019, MNRAS, 487, 3815
Milone, A. P., Cordoni, G., Marino, A. F., et al. 2023b, A&A, 672, A161
Milone, A. P., & Marino, A. F. 2022, Univ, 8, 359
Milone, A. P., Marino, A. F., Bedin, L. R., et al. 2014, MNRAS, 439, 1588
Milone, A. P., Marino, A. F., Bedin, L. R., et al. 2019, MNRAS, 484, 4046
Milone, A. P., Marino, A. F., Cassisi, S., et al. 2012b, ApJL, 754, L34
Milone, A. P., Marino, A. F., Cassisi, S., et al. 2017a, MNRAS, 469, 800
Milone, A. P., Marino, A. F., Da Costa, G. S., et al. 2020, MNRAS, 491, 515
Milone, A. P., Marino, A. F., Dotter, A., et al. 2023a, MNRAS, 522, 2429
Milone, A. P., Marino, A. F., Mastrobuono-Battisti, A., & Lagioia, E. P. 2018a, MNRAS, 479, 5005
Milone, A. P., Marino, A. F., Renzini, A., et al. 2018b, MNRAS, 481, 5098
Milone, A. P., Piotto, G., Bedin, L. R., et al. 2012a, A&A, 537, A77
Milone, A. P., Piotto, G., Renzini, A., et al. 2017b, MNRAS, 464, 3636
Nardiello, D., Griggio, M., & Bedin, L. R. 2023, MNRAS, 521, L39
Nardiello, D., Milone, A. P., Piotto, G., et al. 2018, MNRAS, 477, 2004
Partridge, H., & Schwenke, D. W. 1997, JChPh, 106, 4618
Phillips, M. W., Tremblin, P., Baraffe, I., et al. 2020, A&A, 637, A38
Renzini, A., D'Antona, F., Cassisi, S., et al. 2015, MNRAS, 454, 4197
Renzini, A., Marino, A. F., & Milone, A. P. 2022, MNRAS, 513, 2111
Richer, H. B., Heyl, J., Anderson, J., et al. 2013, ApJL, 771, L15
Sabbi, E., Lennon, D. J., Anderson, J., et al. 2016, ApJS, 222, 11
Sbordone, L., Bonifacio, P., Castelli, F., & Kurucz, R. L. 2004, MSAIS, 5, 93
Sbordone, L., Bonifacio, P., & Castelli, F. 2007, in IAU Symp. 239, Convection in Astrophysics, ed. F. Kupka, I. Roxburgh, & K. L. Chan (Cambridge: Cambridge Univ. Press), 71
Tailo, M., Milone, A. P., Lagioia, E. P., et al. 2020, MNRAS, 498, 5745
VandenBerg, D. A., Edvardsson, B., Casagrande, L., & Ferguson, J. W. 2022, MNRAS, 509, 4189
Ventura, P., D'Antona, F., Mazzitelli, I., & Gratton, R. 2001, ApJL, 550, L65
Wang, L., Kroupa, P., Takahashi, K., & Jerabkova, T. 2020, MNRAS, 491, 440
Zennaro, M., Milone, A. P., Marino, A. F., et al. 2019, MNRAS, 487, 3239
Ziliotto, T., Milone, A., Marino, A. F., et al. 2023, ApJ, 953, 62